Analytic Solutions of Model Predictive Current Control for SPMSM Drives

Jun Zhang, Binyu Xia, and Mingming Zhang, *Member, IEEE*

***Abstract*—In this article, we present analytic solutions for model predictive control (MPC) applied to the current control of surface-mounted permanent magnet synchronous motor drives. A key challenge in applying MPC to motor current control is solving the constrained optimization problem in real time. To address this, we develop an explicit procedure based on planar geometric projections to solve the problem efficiently. The correctness of our method is validated through comparisons with standard numerical solvers. Experimental results demonstrate that our algorithm can be implemented on low-cost hardware with rapid execution, supporting long prediction and control horizons while delivering fast dynamic response and low total harmonic distortion at steady state. These advantages make it suitable for both high-speed servo systems and budget-sensitive applications.**

***Index Terms*—Analytic solutions, model predictive control (MPC), surface-mounted permanent magnet synchronous motor (SPMSM).**

I. Introduction

PERMANENT magnet synchronous motors (PMSMs) are widely used in modern industry due to their high power density, fast dynamic response, and excellent energy efficiency [1]. Typically, PMSMs are controlled using a cascade structure [2], [3], where mechanical variables such as velocity and torque are regulated by an outer loop, while the inner loop controls the current, addressing their distinct time scales. The inner current controller plays an important role in ensuring a prompt dynamic response and maintaining high efficiency across various operating conditions.

Proportional-Integral (PI) algorithm is commonly employed for current control in PMSMs due to its simplicity and low computational demand [2], [3], [4]. Recently, model predictive control (MPC) has seen significant advancements in power electronic system control [5]. MPC strategies for PMSM control can be broadly categorized into direct and indirect approaches. Direct MPC generates switching signals for power electronic devices directly, as seen in finite control set (FCS) MPC [6], [7], [8]. However, the FCS-MPC methods have an intrinsic drawback of variable switching frequency, resulting in undesirable harmonics at steady state. Some methods such as [9], [10] tries to mitigate this problem by using optimization algorithm. However, this issue cannot be fully eliminated, especially when long prediction horizon is used, as discussed in [11]. Indirect MPC, in contrast, produces voltage commands that are fed into a modulator using modulation techniques like space vector pulsewidth modulation (SVPWM), thus masking the inverter switching actions. For indirect MPC, the current reference tracking problem can be formulated as a constrained optimization problem with continuous-time control input at each sampling instant.

Solving this optimization problem in real time can be accomplished using off-the-shelf solvers [12], [13], [14], but this approach imposes heavy computational demands and requires advanced hardware. Explicit MPC (EMPC) reformulates the constrained optimization as a multiparametric Quadratic Programming (mp-QP) problem, where the optimal controls are expressed as piecewise affine functions of the parameter state. By precomputing these solutions offline and storing them in memory, EMPC enables rapid real-time control at high sampling frequencies [15], [16], [17], [18], [19]. However, EMPC becomes challenging with longer prediction and control horizons, even when solved offline, as these horizons are often desired for better control performance [20]. This difficulty arises from the exponential growth in computational complexity as the problem size increases.

In recent years, there have been remarkable advancements in MPC-based controller design for power electronic applications. Martin et al. [21], [22] proposed analytical solutions for a continuous control set MPC problem, significantly enhancing reliability, and reducing computational burden. However, these methods are limited to one-step MPC formulations and, therefore, do not fully exploit the inherent advantages of MPC with longer horizons. Cimini et al.[23] represented the latest advancement in the application of EMPC for power electronic systems. It relies on online optimization with increased computational burden and limits the feasibility of using longer prediction horizons. To summarize, the performance of the MPC is mainly affected by the controller structure, the computational capability, and the length of the predictive horizon. These factors are usually conflicting in practice. For commercial motor drives in the industry, it is demanding to develop an explicit MPC method with a fast dynamic response but at a moderate cost.

Received 23 March 2025; accepted 29 April 2025. Date of publication 5 May 2025; date of current version 30 June 2025. Recommended for publication by Associate Editor Amit K. Gupta. *(Corresponding author: Mingming Zhang.)*

Jun Zhang and Binyu Xia are with UMich-SJTU Joint Institute, Shanghai Jiao Tong University, Shanghai 200240, China (e-mail: zhangjun12@sjtu.edu.cn; xiabinyu@sjtu.edu.cn).

Mingming Zhang is with the Global Institute of Future Technology, Shanghai Jiao Tong University, Shanghai 200240, China (e-mail: brucechang@sjtu.edu.cn).

Color versions of one or more figures in this article are available at https://doi.org/10.1109/TPEL.2025.3567060.

Digital Object Identifier 10.1109/TPEL.2025.3567060

In this article, we present analytic solutions to the constrained optimization problem in MPC, applied to the current control of surface-mounted permanent magnet synchronous motor (SPMSM) drives. Our approach provides a computationally efficient method for determining the control commands of the MPC in real time through simple planar geometric projections. The main advantages of our MPC solution are as follows:

1) All computations are performed using analytic solutions, which require only low computational resources and can be executed rapidly, make it suitable for both high-speed servo systems and budget-sensitive applications.
2) Long prediction and control horizons can be employed to achieve faster dynamic response as well as lower total harmonic distortion (THD) at steady state.

The correctness of our solution is validated by comparisons with established numerical solvers. Experimental results demonstrate that our algorithm can be implemented on low-cost hardware with short computation time, while achieving fast dynamic response. These advantages make it suitable for both high-speed servo systems and cost-sensitive applications.

II. Background

In this section, we present some necessary backgrounds.

A. Mathematical Model of SPMSM

The continuous time current model of PMSM in the rotor coordinate is

$$\frac{d}{dt}\boldsymbol{i}(t) = \boldsymbol{A}_c\boldsymbol{i}(t) + \boldsymbol{B}_c\boldsymbol{u}(t) + \boldsymbol{g}_c \tag{1}$$

where

$$\boldsymbol{A}_c = -\boldsymbol{L}_s^{-1}\begin{bmatrix} R_s & -L_q\omega \\ L_d\omega & R_s \end{bmatrix}, \quad \boldsymbol{L}_s = \begin{bmatrix} L_d & 0 \\ 0 & L_q \end{bmatrix}$$
$$\boldsymbol{B}_c = \boldsymbol{L}_s^{-1}, \quad \boldsymbol{g}_c = -\boldsymbol{L}_s^{-1}\begin{bmatrix} 0 \\ 1 \end{bmatrix}\omega\psi_f.$$

Here, $\boldsymbol{i}$ is the stator current, $\boldsymbol{u}$ the stator voltage, L_d the d-axis inductance, L_q the q-axis inductance, R_s the stator resistance, ω the electrical angular velocity, and ψ_f the permanent magnet flux linkage. In this article, we only study the SPMSM drives and thus $L_d = L_q$.

Discretizing (1) with zero-order holder yields

$$\boldsymbol{i}_{k+1} = \boldsymbol{F}\boldsymbol{i}_k + \boldsymbol{B}\boldsymbol{u}_k + \boldsymbol{g} \tag{2}$$

where

$$\boldsymbol{F} = e^{\boldsymbol{A}_c T_s}$$
$$\boldsymbol{B} = \int_0^{T_s} e^{\boldsymbol{A}_c(T_s-\tau)}\boldsymbol{B}_c d\tau = \boldsymbol{A}_c^{-1}(e^{\boldsymbol{A}_c T_s} - \boldsymbol{I})\boldsymbol{B}_c$$
$$\boldsymbol{g} = \int_0^{T_s} e^{\boldsymbol{A}_c(T_s-\tau)}\boldsymbol{g}_c d\tau = \boldsymbol{A}_c^{-1}(e^{\boldsymbol{A}_c T_s} - \boldsymbol{I})\boldsymbol{g}_c \tag{3}$$

and T_s is the sampling period. Denote the current at the steady state as $\bar{\boldsymbol{i}}$ and the voltage as $\bar{\boldsymbol{u}}$. From (2), we have $\bar{\boldsymbol{i}} = \boldsymbol{F}\bar{\boldsymbol{i}} + \boldsymbol{B}\bar{\boldsymbol{u}} + \boldsymbol{g}$, and therefore $\bar{\boldsymbol{u}} = \boldsymbol{B}^{-1}[(\boldsymbol{I}-\boldsymbol{F})\bar{\boldsymbol{i}} - \boldsymbol{g}]$. Letting $\boldsymbol{x}_k = \boldsymbol{i}_k - \bar{\boldsymbol{i}}$ and $\boldsymbol{v}_k = \boldsymbol{u}_k - \bar{\boldsymbol{u}}$, we obtain a model with no drift input

$$\boldsymbol{x}_{k+1} = \boldsymbol{F}\boldsymbol{x}_k + \boldsymbol{B}\boldsymbol{v}_k. \tag{4}$$

B. Multiparametric Quadratic Programming (mp-QP)

The mp-QP problem is presented as follows (See [19] for more details):

$$\min_{\boldsymbol{\mu}} \boldsymbol{J} = \frac{1}{2}\boldsymbol{\mu}^T\boldsymbol{H}\boldsymbol{\mu} \tag{5a}$$
$$\text{s.t.} \quad \boldsymbol{G}\boldsymbol{\mu} \le \boldsymbol{S}\boldsymbol{x}_0 + \boldsymbol{w} \tag{5b}$$

where $\boldsymbol{\mu}$ is the optimization variable, and $\boldsymbol{x}_0$ is taken as a parameter. To solve this problem, we form the Lagrangian as $L = \frac{1}{2}\boldsymbol{\mu}^T\boldsymbol{H}\boldsymbol{\mu} + \boldsymbol{\lambda}^T(\boldsymbol{G}\boldsymbol{\mu} - \boldsymbol{S}\boldsymbol{x}_0 - \boldsymbol{w})$, where $\boldsymbol{\lambda}$ is the Lagrange multiplier. The Karush–Kuhn–Tucker optimality conditions for the mp-QP are given by

$$\boldsymbol{H}\boldsymbol{\mu}^* + \boldsymbol{G}^T\boldsymbol{\lambda}^* = 0, \ \boldsymbol{\lambda} \in \mathbb{R}^m \tag{6a}$$
$$\boldsymbol{\lambda}_i^*(\boldsymbol{G}_i\boldsymbol{\mu}^* - \boldsymbol{w}_i - \boldsymbol{S}_i\boldsymbol{x}_0) = 0, \ i = 1, \ldots, m \tag{6b}$$
$$\boldsymbol{\lambda}^* \ge 0 \tag{6c}$$
$$\boldsymbol{G}\boldsymbol{\mu}^* - \boldsymbol{w} - \boldsymbol{S}\boldsymbol{x}_0 \le 0. \tag{6d}$$

The primal feasibility condition (6d) can be split into active and inactive constraint parts

$$\boldsymbol{G}_A\boldsymbol{\mu}^* - \boldsymbol{S}_A\boldsymbol{x}_0 = \boldsymbol{w}_A \tag{7a}$$
$$\boldsymbol{G}_{NA}\boldsymbol{\mu}^* - \boldsymbol{S}_{NA}\boldsymbol{x}_0 < \boldsymbol{w}_{NA} \tag{7b}$$

where A and NA are the index sets for active and nonactive constraints, respectively. Let $\boldsymbol{\lambda}_{NA}^*$ and $\boldsymbol{\lambda}_A^*$ denote the Lagrange multipliers corresponding to inactive and active constraints, respectively. We can obtain that

$$\boldsymbol{\lambda}_A^* = -\boldsymbol{T}_d(\boldsymbol{w}_A + \boldsymbol{S}_A\boldsymbol{x}_0) \tag{8}$$
$$\boldsymbol{\mu}^* = -\boldsymbol{H}^{-1}\boldsymbol{G}_A^T\boldsymbol{\lambda}_A^* \tag{9}$$

where $\boldsymbol{T}_d = (\boldsymbol{G}_A\boldsymbol{H}^{-1}\boldsymbol{G}_A^T)^{-1}$. For active constraints, we have $\boldsymbol{\lambda}_A^* \ge 0$ and the dual feasibility region is

$$\mathcal{P}_d^A = \{\boldsymbol{x}_0 \mid \boldsymbol{\lambda}_A^* \ge 0\} = \{\boldsymbol{x}_0 \mid \boldsymbol{T}_d\boldsymbol{S}_A\boldsymbol{x}_0 \le -\boldsymbol{T}_d\boldsymbol{w}_A\}. \tag{10}$$

For inactive constraints, we have $\boldsymbol{\lambda}_{NA}^* = 0$ and the primal feasibility region is

$$\mathcal{P}_p^A = \{\boldsymbol{x}_0 \mid (\boldsymbol{T}_p\boldsymbol{S}_A - \boldsymbol{S}_{NA})\boldsymbol{x}_0 < \boldsymbol{w}_{NA} - \boldsymbol{T}_p\boldsymbol{w}_A\} \tag{11}$$

where $\boldsymbol{T}_p = \boldsymbol{G}_{NA}\boldsymbol{H}^{-1}\boldsymbol{G}_A^T\boldsymbol{T}_d$.

We have the following definition and properties from [19].

Definition 1: Define the critical region CR_A as the set of all parameters $\boldsymbol{x}_0$ such that the active constraints are indexed by A at the optimum.

Property 1: CR_A is the intersection of $\mathcal{P}_p^A$ and $\mathcal{P}_d^A$, *i.e.*, $\mathrm{CR}_A = \mathcal{P}_p^A \cap \mathcal{P}_d^A$.

Property 2: For any two neighboring full-dimensional critical regions CR_{A_i} and CR_{A_j}, we have $A_i \subset A_j$ and $|A_i| = |A_j| - 1$, or $A_j \subset A_i$ and $|A_j| = |A_i| - 1$, where $|\cdot|$ denotes the cardinality (*i.e.*, number) of a set.

C. Model Predictive Control

MPC is an advanced control strategy that is successfully applied across various industries. It utilizes a discrete-time plant model, such as (4), to predict future system outputs $\{\boldsymbol{x}_{k+1}, \cdots, \boldsymbol{x}_{k+N_p}\}$ from a series of control inputs $\{\boldsymbol{v}_k, \cdots, \boldsymbol{v}_{k+N_u-1}\}$, where N_p and N_u are prediction and control horizons, respectively. The control objectives are encoded into a cost function such as that in (5a) with constraints in (5b).

The central idea of MPC is a receding horizon type of control. At each sampling instant, the outputs are measured and the constrained optimization problem is solved. The measured outputs are also compared with the predicted ones to generate error signals that are fed into the model to enhance the prediction accuracy and eliminate any offsets. At the next sampling instant, the first control input from the optimization is applied to the plant, and the whole procedure is repeated for newly measured outputs. As time progresses, the prediction and control horizons shift forward, continuously updating the control strategy.

MPC offers superior control performance with fast response times and strong robustness against uncertainties. However, the requirement for online optimization at each sampling instant can be computationally intensive, especially for larger problems or systems with complex constraints. This computational burden can restrict the prediction and control horizons and limit the feasibility of MPC in high-speed systems or on low-cost hardware platforms.

III. MP-QP Formulation for SPMSM Predictive Current Control

We now show that the predictive current control for SPMSM can be formulated as an mp-QP problem that needs to be solved in real time at each sampling instant.

To achieve a given reference current $\boldsymbol{i}_{\text{ref}}$, we can choose the steady state current $\bar{\boldsymbol{i}} = \boldsymbol{i}_{\text{ref}}$ and then the current tracking error $\boldsymbol{x}_k = \boldsymbol{i}_k - \boldsymbol{i}_{\text{ref}}$. The mathematical model of SPMSM is represented by (4). The current set-point tracking can be formulated as the following least quadratic regulation (LQR) problem

$$\min_{\boldsymbol{v}_k} \quad J_0 = \sum_{k=1}^{N} \frac{1}{2}\boldsymbol{x}_k^T \boldsymbol{Q}\boldsymbol{x}_k + \sum_{k=0}^{N-1} \frac{1}{2}\boldsymbol{v}_k^T \boldsymbol{R}\boldsymbol{v}_k \tag{12a}$$

$$\text{s.t.} \quad \boldsymbol{x}_{k+1} = \boldsymbol{F}\boldsymbol{x}_k + \boldsymbol{B}\boldsymbol{v}_k,\ k = 0, 1, \ldots, N-1 \tag{12b}$$

$$\boldsymbol{x}_0 = \boldsymbol{i}(0) - \bar{\boldsymbol{i}} \tag{12c}$$

$$\boldsymbol{v}_k \in \mathcal{U}_k,\ k = 0, 1, \ldots, N-1 \tag{12d}$$

$$\boldsymbol{x}_k \in \mathcal{X}_k,\ k = 1, \ldots, N, \tag{12e}$$

where $\boldsymbol{Q}$ and $\boldsymbol{R}$ are positive semi-definite matrices.

From the receding horizon nature of MPC, we always take the current time instant as $t = t_0$ and consider the N future control actions $\boldsymbol{v}_0, \ldots, \boldsymbol{v}_{N-1}$ and the resulting states $\boldsymbol{x}_1, \ldots, \boldsymbol{x}_N$. In the cost function (12a), minimizing the term $\sum_{k=1}^{N} \frac{1}{2}\boldsymbol{x}_k^T \boldsymbol{Q}\boldsymbol{x}_k$ will reduce the tracking errors, effectively driving the current to track $\boldsymbol{i}_{\text{ref}}$, and the term $\sum_{k=0}^{N-1} \frac{1}{2}\boldsymbol{v}_k^T \boldsymbol{R}\boldsymbol{v}_k$ represents a penalty on the control action. Equation (12b) is the dynamical equation of the current tracking error in dq-axis, and $\boldsymbol{i}(0)$ in (12c) is the measured current at the present moment. In (12d) and (12e), $\mathcal{U}_k$ and $\mathcal{X}_k$ are the constraints for $\boldsymbol{v}_k$ and $\boldsymbol{x}_k$, respectively.

The MPC algorithm needs to solve the constrained optimization problem (12) based on the measured current $\boldsymbol{i}(0)$ in real time, and to apply only the first control $\boldsymbol{v}_0$. The same procedure will be repeated at each sampling instant as time evolves. In the rest of this section, we will first discuss the details of the constraints for the inputs and states, and then translate (12) into an mp-QP problem.

A. Constraints on the Control Inputs

Consider a motor driven by power electronic devices using SVPWM, a widely applied modulating scheme. To fully utilize the control boundary within the SVPWM scheme, the constrained set for the input voltage $\boldsymbol{u}_{\alpha\beta}$ is a regular hexagon defined by $\{\boldsymbol{u}_{\alpha\beta} \in \mathbb{R}^2 \mid \boldsymbol{A}_u \boldsymbol{u}_{\alpha\beta} \le \boldsymbol{b}_u\}$, where $\boldsymbol{A}_u \in \mathbb{R}^{6\times 2}$ and its mth row is

$$\boldsymbol{A}_u^m = \left[\cos\tfrac{2m-1}{6}\pi, \quad \sin\tfrac{2m-1}{6}\pi\right],\ m = 1, \ldots, 6 \tag{13}$$

and $\boldsymbol{b}_u = \frac{\sqrt{3}}{2} b \mathbf{1}_6$, $b = \frac{2}{3}V_{dc}$, $\mathbf{1}_6$ is the vector in $\mathbb{R}^6$ whose the elements are all 1. The equation $\boldsymbol{A}_u^m \boldsymbol{u}_{\alpha\beta} = \frac{\sqrt{3}}{2} b$ defines an edge of the regular hexagon, where $\boldsymbol{A}_u^m$ gives its unit normal vector, and the distance from the origin to this edge is $\frac{\sqrt{3}}{2} b$.

To transform this constraint from $\alpha\beta$-frame into dq-frame, we suppose that at the present moment the motor angular position is θ and the velocity ω. Because $\boldsymbol{u}_{dq} = R(-\theta)\boldsymbol{u}_{\alpha\beta}$, the voltage constraints can then be represented by $\boldsymbol{A}_u R(\theta)\boldsymbol{u}_{dq} \le \boldsymbol{b}_u$.

Equation (12d) represents the voltage constraints on all the future time instants from t_0 to t_{N-1}. We now transform them into a vector form. Because the time scale of electrical part is much smaller than that of mechanical part, the angular position at future time instant $t_0 + kT_s$ can be approximated by $\theta + k\omega T_s$, where $k = 0, 1, \cdots, N-1$. Therefore, the constraints on future input voltages are

$$\boldsymbol{A}_u R(\theta + k\omega T_s)\boldsymbol{u}_k \le \boldsymbol{b}_u. \tag{14}$$

Letting

$$\mathcal{A}_v = \text{diag}\{\boldsymbol{A}_u R(\theta), \boldsymbol{A}_u R(\theta + \omega T_s) \cdots, \boldsymbol{A}_u R(\theta + (N-1)\omega T_s)\} \tag{15}$$

we can rewrite (14) collectively as

$$\mathcal{A}_v \boldsymbol{V}_0 \le \mathbf{1}_N \otimes \boldsymbol{b}_u - \mathcal{A}_v(\mathbf{1}_N \otimes \bar{\boldsymbol{u}}) \tag{16}$$

where $\boldsymbol{V}_0 = [\boldsymbol{v}_0, \quad \cdots, \quad \boldsymbol{v}_{N-1}]^T$, and $\otimes$ denotes the tensor (aka Kronecker) product. The constraints on all the control voltages at future time instants in (12d) can now be represented by (16).

B. Constraints on the Future States

In motor control, it is common practice to impose a bound on the magnitude of the current vector. When this bound is exceeded, a protective mechanism is activated to safeguard the motor. We assume the current vector is constrained within a circle, *i.e.*, $\|\boldsymbol{i}\|_2 \le I_{\max}$, where $I_{\max}$ represents the bound. To simplify the analysis, we approximate the circular boundary

using a regular N_i-gon, defined by $\{\boldsymbol{i} \in \mathbb{R}^2 \mid \boldsymbol{A}_i \boldsymbol{i} \leq \boldsymbol{b}_i\}$, where N_i is a large integer, $\boldsymbol{A}_i \in \mathbb{R}^{N_i \times 2}$, and its nth row is

$$\boldsymbol{A}_i^n = \left[\cos \tfrac{2n-1}{N_i}\pi, \quad \sin \tfrac{2n-1}{N_i}\pi\right], \; n = 1, \ldots, N_i.$$

Here, we select $N_i = 12$ to tradeoff the approximation accuracy and constraints complexity. Then, the future tracking errors $\boldsymbol{x}_k$ has to satisfy

$$\boldsymbol{A}_i \boldsymbol{x}_k = \boldsymbol{A}_i \boldsymbol{i}_k - \boldsymbol{A}_i \bar{\boldsymbol{i}} \leq \boldsymbol{b}_i - \boldsymbol{A}_i \bar{\boldsymbol{i}} \triangleq \boldsymbol{b}_x \tag{17}$$

where $k = 1, \cdots, N$. From (12b), $\boldsymbol{x}_k$ can be obtained as

$$\boldsymbol{x}_k = \boldsymbol{F}^k \boldsymbol{x}_0 + \boldsymbol{F}^{k-1}\boldsymbol{B}\boldsymbol{v}_0 + \cdots + \boldsymbol{B}\boldsymbol{v}_{k-1}.$$

Putting all the equations of $\boldsymbol{x}_k$ together, we can obtain

$$\underbrace{\begin{bmatrix} \boldsymbol{x}_1 \\ \boldsymbol{x}_2 \\ \vdots \\ \boldsymbol{x}_N \end{bmatrix}}_{\mathcal{X}} = \underbrace{\begin{bmatrix} \boldsymbol{F} \\ \boldsymbol{F}^2 \\ \vdots \\ \boldsymbol{F}^N \end{bmatrix}}_{\mathcal{S}_x} \boldsymbol{x}_0 + \underbrace{\begin{bmatrix} \boldsymbol{B} & & & \\ \boldsymbol{F}\boldsymbol{B} & \boldsymbol{B} & & \\ \vdots & \ddots & \ddots & \\ \boldsymbol{F}^{N-1}\boldsymbol{B} & \cdots & \boldsymbol{F}\boldsymbol{B} & \boldsymbol{B} \end{bmatrix}}_{\mathcal{S}_u} \underbrace{\begin{bmatrix} \boldsymbol{v}_0 \\ \boldsymbol{v}_1 \\ \vdots \\ \boldsymbol{v}_{N-1} \end{bmatrix}}_{\boldsymbol{V}_0}. \tag{18}$$

The constraints in (17) can be compactly written as

$$(\boldsymbol{I}_N \otimes \boldsymbol{A}_i)\mathcal{X} = (\boldsymbol{I}_N \otimes \boldsymbol{A}_i)(\mathcal{S}_x \boldsymbol{x}_0 + \mathcal{S}_u \boldsymbol{V}_0) \leq \boldsymbol{1}_N \otimes \boldsymbol{b}_x$$

where $\boldsymbol{I}_N$ is the identity matrix in $\mathbb{R}^{N \times N}$. Since future states are generated by future control voltages, this constraint can in turn be transformed to constraints on the voltage vector $\boldsymbol{V}_0$:

$$(\boldsymbol{I}_N \otimes \boldsymbol{A}_i)\mathcal{S}_u \boldsymbol{V}_0 \leq -(\boldsymbol{I}_N \otimes \boldsymbol{A}_i)\mathcal{S}_x \boldsymbol{x}_0 + \boldsymbol{1}_N \otimes \boldsymbol{b}_x. \tag{19}$$

The constraints on all the states at future time instants in (12e) is now characterized by (19).

C. mp-QP Problem Formulation

We now combine the two constraints in (16) and (19) as

$$\boldsymbol{G}\boldsymbol{V}_0 \leq \boldsymbol{E}\boldsymbol{x}_0 + \boldsymbol{w} \tag{20}$$

where

$$\boldsymbol{G} = \begin{bmatrix} \mathcal{A}_v \\ (\boldsymbol{I}_N \otimes \boldsymbol{A}_i)\mathcal{S}_u \end{bmatrix}, \quad \boldsymbol{E} = \begin{bmatrix} \boldsymbol{0} \\ -(\boldsymbol{I}_N \otimes \boldsymbol{A}_i)\mathcal{S}_x \end{bmatrix}$$
$$\boldsymbol{w} = \begin{bmatrix} \boldsymbol{1}_N \otimes \boldsymbol{b}_u - \mathcal{A}_v(\boldsymbol{1}_N \otimes \bar{\boldsymbol{u}}) \\ \boldsymbol{1}_N \otimes \boldsymbol{b}_x \end{bmatrix}. \tag{21}$$

For simplicity, MPC implementations often select $\boldsymbol{Q}$ and $\boldsymbol{R}$ as diagonal matrices with identical diagonal entries. In particular, let $\boldsymbol{Q} = 1/s_B^2 \boldsymbol{I}$ and $\boldsymbol{R} = r\boldsymbol{I}$. Here, s_B is a constant determined by the motor's physical parameters [as will be defined in (25)], making r a tuning parameter. Substituting these two equations and (18) into the cost function J_0 in (12a), we get

$$\begin{aligned} J_0 &= \frac{1}{2s_B^2}\mathcal{X}^T\mathcal{X} + \frac{r}{2}\boldsymbol{V}_0^T\boldsymbol{V}_0 \\ &= \frac{1}{2s_B^2}\left(\mathcal{S}_x\boldsymbol{x}_0 + \mathcal{S}_u\boldsymbol{V}_0\right)^T\left(\mathcal{S}_x\boldsymbol{x}_0 + \mathcal{S}_u\boldsymbol{V}_0\right) + \frac{r}{2}\boldsymbol{V}_0^T\boldsymbol{V}_0 \\ &= \frac{1}{2}\boldsymbol{V}_0^T\boldsymbol{H}\boldsymbol{V}_0 + \boldsymbol{x}_0^T\boldsymbol{M}\boldsymbol{V}_0 + \frac{1}{2}\boldsymbol{x}_0^T\boldsymbol{Y}\boldsymbol{x}_0 \end{aligned}$$

where $\boldsymbol{H} = \mathcal{S}_u^T\mathcal{S}_u/s_B^2 + r\boldsymbol{I}$, $\boldsymbol{M} = {\mathcal{S}_x}^T\mathcal{S}_u/s_B^2$, and $\boldsymbol{Y} = {\mathcal{S}_x}^T\mathcal{S}_x/s_B^2$. Letting $\boldsymbol{\mu} \triangleq \boldsymbol{V}_0 + \boldsymbol{H}^{-1}\boldsymbol{M}^T\boldsymbol{x}_0$, we can get

$$J_0 = \frac{1}{2}\boldsymbol{\mu}^T\boldsymbol{H}\boldsymbol{\mu} + \frac{1}{2}\boldsymbol{x}_0^T(\boldsymbol{Y} - \boldsymbol{M}\boldsymbol{H}^{-1}\boldsymbol{M})\boldsymbol{x}_0. \tag{22}$$

The initial state $\boldsymbol{x}_0$ is obtained from measurement, and thus the second term in (22) is a constant and can be discarded from the optimization. We can now transform the LQR problem in (12) to an equivalent mp-QP problem as follows:

$$\min_{\boldsymbol{\mu}} J = \frac{1}{2}\boldsymbol{\mu}^T\boldsymbol{H}\boldsymbol{\mu} \tag{23a}$$
$$\text{s.t.} \boldsymbol{G}\boldsymbol{\mu} \leq \boldsymbol{S}\boldsymbol{x}_0 + \boldsymbol{w} \tag{23b}$$

where $\boldsymbol{S} = \boldsymbol{E} + \boldsymbol{G}\boldsymbol{H}^{-1}\boldsymbol{M}^T$.

D. Properties of $\boldsymbol{F}$ and $\boldsymbol{B}$

For the SPMSM under study, we let $L_s = L_d = L_q$. The matrices $\boldsymbol{F}$ and $\boldsymbol{B}$ in (3) can both be expressed as a rotation matrix multiplied with a scalar (SRM). Explicit computation yields that

$$\boldsymbol{F} = e^{-\frac{R_s T_s}{L_s}} \begin{bmatrix} \cos\omega T_s & \sin\omega T_s \\ -\sin\omega T_s & \cos\omega T_s \end{bmatrix} = s_F R(-\omega T_s) \tag{24}$$

where $s_F = e^{-\frac{R_s T_s}{L_s}} < 1$, and $R(\cdot)$ is the rotation matrix. Hence, $\boldsymbol{F}$ is the product of rotation matrix $R(-\omega T_s)$ and the scalar s_F. We can also show that $\boldsymbol{B} = s_B R(\theta_B)$, where

$$\begin{aligned} s_B &= \sqrt{\frac{e^{-2R_s/L_s T_s} - 2e^{-R_s/L_s T_s}\cos\omega T_s + 1}{R_s^2 + \omega^2 L_s^2}} \\ \theta_B &= \operatorname{atan2}\Big(e^{-\frac{R_s T_s}{L_s}}(\omega L_s \sin\omega T_s - R_s\cos\omega T_s) + R_s \\ &\qquad e^{-\frac{R_s T_s}{L_s}}(\omega L_s\cos\omega T_s + R_s\sin\omega T_s) - \omega L_s\Big) \end{aligned} \tag{25}$$

and atan2 is the four-quadrant tangent inverse. Then $\boldsymbol{B}$ is the product of rotation matrix $R(\theta_B)$ and the scalar s_B. It is clear that both $\boldsymbol{F}$ and $\boldsymbol{B}$ are 2×2 SRMs and they satisfy $\boldsymbol{F}^T\boldsymbol{F} = s_F^2\boldsymbol{I}$ and $\boldsymbol{B}^T\boldsymbol{B} = s_B^2\boldsymbol{I}$. An important property for $\boldsymbol{F}$ and $\boldsymbol{B}$ is that they commute, *i.e.*, $\boldsymbol{B}\boldsymbol{F} = \boldsymbol{F}\boldsymbol{B}$. In later discussions, we will see that this property makes it possible to derive the analytic solutions.

IV. Analytic Solutions to Predictive Current Control

We begin by presenting our analytic procedure for solving the control commands of the MPC applied to SPMSM current control, followed by the mathematical derivations. This approach provides readers with a clear idea on how to implement the algorithm. While the derivation process is complicated, the resulting control algorithm is simple and easy to implement. For readers not interested in the detailed mathematical steps, the analytic solution can be directly applied to control the motor by following the procedures presented in Section IV-A, without needing to delve into the underlying mathematics.

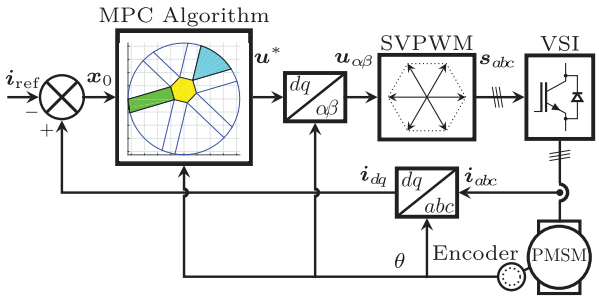

Fig. 1. Block diagram for analytic implementation of MPC for SPMSM current control.

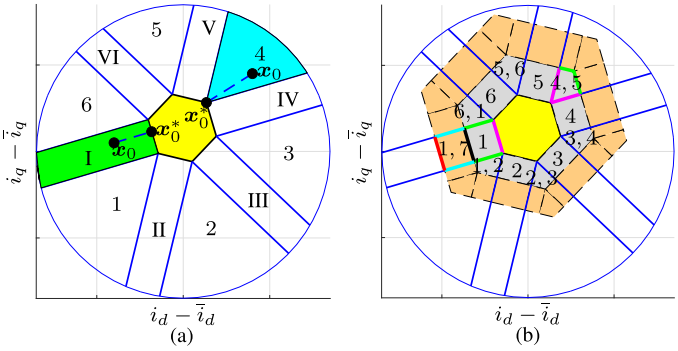

Fig. 2. (a) Geometric interpretation of MPC implementation in the plane of motor currents; (b) The detailed distribution of critical regions.

A. Analytic Implementation of MPC Current Control

We present the main result of this article, that is, the analytic implementation of predictive current control. Assume that the motor runs at the speed ω. The SPMSM discrete model can be computed online by (24) and (25). The diagram of MPC for motor current control is illustrated in Fig. 1, and the detailed procedure is described as follows:

1) At the current sampling instant, measure the motor phase current $\boldsymbol{i}_{abc}$, get the angular position θ (sensor) or its estimation $\hat{\theta}$ (sensor-less).
2) Transform $\boldsymbol{i}_{abc}$ into $\boldsymbol{i}_0$ in the dq-frame, and subtract $\boldsymbol{i}_{\text{ref}}$ to form tracking error $\boldsymbol{x}_0$.
3) Compute control zones partitioned as in Fig. 2(a).
   a) The blue circle depicts the magnitude constrain on the current vector, *i.e.*, $\|\boldsymbol{i}\|_2 \leq I_{\max}$.
   b) The yellow hexagon is given by (31a).
   c) The edges of spike-like zones are perpendicular to the corresponding edges of the yellow hexagon.
4) Get the equivalent control state $\boldsymbol{x}_0^*$ from $\boldsymbol{x}_0$:
   a) if $\boldsymbol{x}_0$ is in the yellow hexagon, let $\boldsymbol{x}_0^* = \boldsymbol{x}_0$;
   b) if $\boldsymbol{x}_0$ is in a pie region such as cyan area, let $\boldsymbol{x}_0^*$ be the vertex;
   c) if $\boldsymbol{x}_0$ is in a long strip region such as green area, let $\boldsymbol{x}_0^*$ be its projection to the neighboring hexagon edge.
5) Calculate the control input at the present moment by $\boldsymbol{v}_0^* = -[\boldsymbol{I}, \boldsymbol{0}, \ldots, \boldsymbol{0}]\boldsymbol{H}^{-1}\boldsymbol{M}^T\boldsymbol{x}_0^*$, and apply $\boldsymbol{u}_0^* = \boldsymbol{v}_0^* + \bar{\boldsymbol{u}}$.
6) Repeat Steps 1–5 as time evolves to form a receding horizon control.

B. Partition of Feasible Region Into Control Zones

The core of our analytic solution lies in Step 3, which partitions the feasible region of motor currents in dq-frame, represented by the interior of the blue circle in Fig. 2, into control zones. Among these, the inner yellow hexagon encompasses all states $\boldsymbol{x}_0$, where none of the constraints are active. Each spoke-like zone (e.g. the green area) or wedge-like zone (e.g. the cyan area) represents states with the same active control constraints at the present moment, although their future active control constraints may differ. In this section, we provide an intuitive and constructive description on how this partition is obtained.

Fig. 2(b) shows a finer structure of control zones, where each cell represents a critical region, with numbers inside indicating the associated active sets. Recall that all states within a critical region share the same set of active constraints. We consider constraints on both the input voltage and motor current, with time spanning from the present moment t_0 to the future time instant t_{N-1}. In the following, we describe the procedure for deriving these cells and forming the control zones.

1) No active constraints. This is the simplest case. From Property 1, the critical region is determined by the intersection of dual feasibility region (10) and primal feasibility region (11), which is derived as the inner yellow hexagon in Fig. 2(b) in Section IV-C. Equation (23) becomes an unconstrained optimization problem.
2) Active constraints at $t = t_0$. Using Property 2, Section IV-D first shows that each edge of the yellow hexagon neighbors a rectangular critical region with active set $\{m\}$, for $m = 1, \cdots, 6$, representing the mth sector in the SVPWM hexagon is constrained.
   Next, since the number of active constraints for a wedge-like area can only increase by 1 from that of its neighbors, its active set must be the union of two neighboring active sets. For example, the wedge-like area between rectangular areas $\{4\}$ and $\{5\}$ has active set $\{4, 5\}$, as shown in Fig. 2(b). Its two magenta boundaries are defined by the dual condition, while the two green boundaries are determined by the primal condition. Together, these rectangular and wedge-like areas form the gray zone, which consists of states with active constraints only at $t = t_0$.
3) Active constraints at $t = t_0$ and $t = t_1$. By computing the dual and primal conditions, we can derive that the active set for the rectangular area outside $\{1\}$ is $\{1, 7\}$, representing the 1st sector in the SVPWM hexagon is constrained at both $t = t_0$ and $t = t_1$. Proceeding further, all the critical regions with active constraints at these two time instants form the orange zone.
4) Active constraints at $t = t_0, \cdots, t_{N-1}$. We progressively compute the critical regions for active constraints at more future time instants, getting more zones until they cover the entire blue current circle.

For critical regions with active sets $\{1\}$, $\{1,7\}$, and $\{1,7,13\}$, they all have the same active constraint 1 at $t=t_0$, and all states along the line perpendicular to the yellow hexagon edge have the same first control input. Since MPC applies only the first control, these regions can be combined into the green spoke zone in Fig. 2(a). Similarly, all critical regions with the active set of $\{4,5\}$ at $t=t_0$ can be combined into the cyan zone.

The rest of this section will discuss the technical details involved in deriving the control zones.

C. Yellow Hexagon for No Active Constraints

We show that when there is no active constraint, the critical region is given by the innermost yellow hexagon. In this case, the control is given by $\boldsymbol{V}_0^* = -\boldsymbol{H}^{-1}\boldsymbol{M}^T\boldsymbol{x}_0$. Because both $\boldsymbol{F}$ and $\boldsymbol{B}$ are SRMs and they commute, we obtain from (18)

$$\boldsymbol{H} = \frac{1}{s_B^2}\mathcal{S}_u^T\mathcal{S}_u + r\boldsymbol{I} = \begin{bmatrix} (r+1+\cdots+s_F^{2N-2})\boldsymbol{I} & \cdots & (\boldsymbol{F}^T)^{N-1} \\ \vdots & \ddots & \vdots \\ \boldsymbol{F}^{N-1} & \cdots & (r+1)\boldsymbol{I} \end{bmatrix}.$$

Notice that $\boldsymbol{H}$ is symmetric and contains only $\boldsymbol{F}$, $\boldsymbol{F}^T$, and their powers. So does $\boldsymbol{H}^{-1}$, and it can be written as

$$\boldsymbol{H}^{-1} = \frac{1}{d_H}\begin{bmatrix} l_{11}\boldsymbol{I} & l_{21}\boldsymbol{F}^T & \cdots & l_{N1}(\boldsymbol{F}^T)^{N-1} \\ l_{21}\boldsymbol{F} & l_{22}\boldsymbol{I} & \cdots & l_{N2}(\boldsymbol{F}^T)^{N-2} \\ \vdots & \vdots & \ddots & \vdots \\ l_{N1}\boldsymbol{F}^{N-1} & l_{N2}(\boldsymbol{F}^T)^{N-2} & \cdots & l_{NN}\boldsymbol{I} \end{bmatrix} \tag{26}$$

where $d_H = \sqrt{\det \boldsymbol{H}}$. Moreover, we have

$$\boldsymbol{H}^{-1}\boldsymbol{M}^T = \boldsymbol{H}^{-1}(\boldsymbol{H}-r\boldsymbol{I})\mathcal{S}_u^{-1}\mathcal{S}_x = (\boldsymbol{I}-r\boldsymbol{H}^{-1})\mathcal{S}_u^{-1}\mathcal{S}_x.$$

Because

$$\mathcal{S}_u{}^{-1}\mathcal{S}_x = \begin{bmatrix} \boldsymbol{B}^{-1} & & & \\ -\boldsymbol{B}^{-1}\boldsymbol{F} & \boldsymbol{B}^{-1} & & \\ & \ddots & \ddots & \\ & -\boldsymbol{B}^{-1}\boldsymbol{F} & \boldsymbol{B}^{-1} \end{bmatrix}\begin{bmatrix} \boldsymbol{F} \\ \boldsymbol{F}^2 \\ \vdots \\ \boldsymbol{F}^N \end{bmatrix} = \begin{bmatrix} \boldsymbol{B}^{-1}\boldsymbol{F} \\ \boldsymbol{0} \\ \vdots \\ \boldsymbol{0} \end{bmatrix}$$

the optimal control is given by

$$\boldsymbol{V}_0^* = -\boldsymbol{H}^{-1}\boldsymbol{M}^T\boldsymbol{x}_0 = \left(r\boldsymbol{H}^{-1}-\boldsymbol{I}\right)\begin{bmatrix} \boldsymbol{B}^{-1}\boldsymbol{F} \\ \boldsymbol{0} \\ \vdots \\ \boldsymbol{0} \end{bmatrix}\boldsymbol{x}_0 = \frac{-1}{d_H}\begin{bmatrix} p_1\boldsymbol{F} \\ p_2\boldsymbol{F}^2 \\ \vdots \\ p_N\boldsymbol{F}^N \end{bmatrix}\boldsymbol{B}^{-1}\boldsymbol{x}_0 \tag{27}$$

where $p_1 = d_H - rl_{11}$, $p_2 = -rl_{21}$, $\cdots$, $p_N = -rl_{N1}$. From the MPC strategy, we apply only the first control, i.e.,

$$\boldsymbol{v}_0^* = \frac{-p_1}{d_H}\boldsymbol{F}\boldsymbol{B}^{-1}\boldsymbol{x}_0 = \frac{-p_1 s_F}{d_H s_B}R\left(-\omega T_s-\theta_B\right)\boldsymbol{x}_0. \tag{28}$$

Next, we derive the boundary for this critical region. The dual feasibility condition (10) is trivially satisfied, and the critical region is solely determined by the primal feasibility condition (11), which can be rewritten as

$$\mathcal{P}_p = \left\{\boldsymbol{x}_0 \mid -\left(\boldsymbol{E}+\boldsymbol{G}\boldsymbol{H}^{-1}\boldsymbol{M}^T\right)\boldsymbol{x}_0 < \boldsymbol{w}\right\}. \tag{29}$$

The inequality in (29) consists of the following two inequalities:

$$-\mathcal{A}_v\boldsymbol{H}^{-1}\boldsymbol{M}^T\boldsymbol{x}_0 \le \boldsymbol{1}_N\otimes\boldsymbol{b}_u - \mathcal{A}_v(\boldsymbol{1}_N\otimes\bar{\boldsymbol{u}}) \tag{30a}$$

$$(\boldsymbol{I}_N\otimes\boldsymbol{A}_i)(\mathcal{S}_x - \mathcal{S}_u\boldsymbol{H}^{-1}\boldsymbol{M}^T)\boldsymbol{x}_0 \le \boldsymbol{1}_N\otimes\boldsymbol{b}_x. \tag{30b}$$

The inequality (30a) can be written as

$$-\mathcal{A}_v\boldsymbol{H}^{-1}\boldsymbol{M}^T\boldsymbol{x}_0 = \frac{-1}{d_H s_B}\begin{bmatrix} p_1 s_F\boldsymbol{A}_u \\ p_2 s_F^2\boldsymbol{A}_u \\ \vdots \\ p_N s_F^N\boldsymbol{A}_u \end{bmatrix}R(\theta-\omega T_s-\theta_B)\boldsymbol{x}_0 < \begin{bmatrix} \boldsymbol{b}_u - \boldsymbol{A}_u R(\theta)\bar{\boldsymbol{u}} \\ \boldsymbol{b}_u - \boldsymbol{A}_u R(\theta+\omega T_s)\bar{\boldsymbol{u}} \\ \vdots \\ \boldsymbol{b}_u - \boldsymbol{A}_u R(\theta+(N-1)\omega T_s)\bar{\boldsymbol{u}} \end{bmatrix}$$

which is equivalent to

$$\boldsymbol{A}_u R(\theta-\omega T_s-\theta_B+\pi)\left(\boldsymbol{x}_0 - \frac{d_H s_B}{p_1 s_F}R(\omega T_s+\theta_B)\bar{\boldsymbol{u}}\right) < \frac{d_H s_B}{p_1 s_F}\boldsymbol{b}_u \tag{31a}$$

$$\vdots$$

$$\boldsymbol{A}_u R(\theta-\omega T_s-\theta_B+\pi)\left(\boldsymbol{x}_0 - \frac{d_H s_B}{p_N s_F^N}R(N\omega T_s+\theta_B)\bar{\boldsymbol{u}}\right) < \frac{d_H s_B}{p_N s_F^N}\boldsymbol{b}_u. \tag{31b}$$

The inequalities in (31) define a set of regular hexagons with the same orientation angle $-(\theta-\omega T_s-\theta_B+\pi)$, and the kth one is centered at $\frac{d_H s_B}{p_k s_F^k}R(k\omega T_s+\theta_B)\bar{\boldsymbol{u}}$ with the side length $\frac{d_H s_B}{p_k s_F^k}\frac{2}{3}V_{dc}$. Extensive numerical computations show that this is a progressively larger set of hexagons, and (31a) defines the innermost yellow hexagon in Fig. 2.

For the inequality (30b), we get from (27)

$$\begin{bmatrix} \boldsymbol{x}_1 \\ \boldsymbol{x}_2 \\ \vdots \\ \boldsymbol{x}_N \end{bmatrix} = \mathcal{S}_x\boldsymbol{x}_0 + \mathcal{S}_u\boldsymbol{V}_0^* = \begin{bmatrix} (1-\frac{p_1}{d_H})\boldsymbol{F}\boldsymbol{x}_0 \\ (1-\frac{p_1+p_2}{d_H})\boldsymbol{F}^2\boldsymbol{x}_0 \\ \vdots \\ (1-\frac{p_1+\cdots+p_N}{d_H})\boldsymbol{F}^N\boldsymbol{x}_0 \end{bmatrix}. \tag{32}$$

Since $\{p_k\}$ is positive, decreasing, and $\sum_{k=1}^N p_k = d_H - r^N$, the norm of $\boldsymbol{x}_k$ is decreasing. Hence, the predicted states all stay within the current circle and (30b) is satisfied.

D. Gray Regions for One or Two Active Constraints Only at the Present Moment

From the property of critical regions in Section II-B, we know that the full-dimensional critical regions neighboring yellow

hexagon can have only one active constraint. We show that these correspond to rectangular gray regions in Fig. 2(b).

Consider the case when one constraint on $\boldsymbol{V}_0^*$ is active at the present moment. From (13) and (15), we can write this constraint as

$$\boldsymbol{G}_A\boldsymbol{V}_0^* - b_0 = 0 \tag{33}$$

where

$$\boldsymbol{G}_A = \begin{bmatrix}\boldsymbol{m}^T R(\theta), & 0, & \cdots, & 0\end{bmatrix}$$
$$\boldsymbol{m}^T = \begin{bmatrix}\cos\frac{2m-1}{6}\pi, & \sin\frac{2m-1}{6}\pi\end{bmatrix}, \text{for some } 1 \le \mathrm{m} \le 6$$
$$b_0 = \frac{\sqrt{3}}{2}b - \boldsymbol{m}^T R(\theta)\bar{\boldsymbol{u}}.$$

Without loss of generality, we consider the case when $m = 1$. Hence $\boldsymbol{G}_A$ is the first row in $\boldsymbol{G}$. For the dual condition (10), we have

$$\boldsymbol{T}_d = (\boldsymbol{G}_A\boldsymbol{H}^{-1}\boldsymbol{G}_A^T)^{-1} = \frac{d_H}{l_{11}},\ \boldsymbol{S}_A = \boldsymbol{G}_A\boldsymbol{H}^{-1}\boldsymbol{M}^T,\ \boldsymbol{w}_A = b_0.$$

Equation (10) becomes

$$\mathcal{P}_d = \left\{\boldsymbol{x}_0 \mid \boldsymbol{G}_A\boldsymbol{H}^{-1}\boldsymbol{M}^T\boldsymbol{x}_0 \le -\frac{\sqrt{3}}{2}b + \boldsymbol{m}^T R(\theta)\bar{\boldsymbol{u}}\right\}.$$

From (27), we have

$$\begin{aligned}\boldsymbol{G}_A\boldsymbol{H}^{-1}\boldsymbol{M}^T\boldsymbol{x}_0 &= \frac{p_1 s_F}{d_H s_B}\boldsymbol{m}^T R(\theta - \omega T_s - \theta_B)\boldsymbol{x}_0 \\ &\le -\frac{\sqrt{3}}{2}b + \boldsymbol{m}^T R(\theta)\bar{\boldsymbol{u}}\end{aligned}$$

which can be rewritten as

$$\boldsymbol{m}^T R(\theta - \omega T_s - \theta_B + \pi)\left(\boldsymbol{x}_0 - \frac{d_H s_B}{p_1 s_F}R(\omega T_s + \theta_B)\bar{\boldsymbol{u}}\right) \ge \frac{d_H s_B}{p_1 s_F}\frac{\sqrt{3}}{2}b. \tag{34}$$

Comparing with (31a), we know that (34) defines a shared boundary with the yellow hexagon, shown as the magenta edge of the hexagon in Fig. 2(b).

For the primal condition (11), we have

$$\boldsymbol{T}_p = \boldsymbol{G}_{NA}\boldsymbol{H}^{-1}\boldsymbol{G}_A\frac{d_H}{l_{11}},\ \boldsymbol{S}_{NA} = \boldsymbol{G}_{NA}\boldsymbol{H}^{-1}\boldsymbol{M}^T.$$

Then, (11) becomes

$$\mathcal{P}_p = \left\{\boldsymbol{x}_0 \mid \boldsymbol{G}_{NA}\left(\boldsymbol{H}^{-1}\boldsymbol{G}_A^T\boldsymbol{G}_A\frac{d_H}{l_{11}} - \boldsymbol{I}\right)\boldsymbol{H}^{-1}\boldsymbol{M}^T\boldsymbol{x}_0 < \boldsymbol{w}_{NA} - \boldsymbol{G}_{NA}\boldsymbol{H}^{-1}\boldsymbol{G}_A\frac{d_H}{l_{11}}\boldsymbol{w}_A\right\}. \tag{35}$$

From (26), we have

$$\boldsymbol{H}^{-1}\boldsymbol{G}_A^T\boldsymbol{G}_A\frac{d_H}{l_{11}} - \boldsymbol{I} = \begin{bmatrix} R(-\theta)(\boldsymbol{m}\boldsymbol{m}^T - \boldsymbol{I})R(\theta) & & & \\ \frac{l_{21}}{l_{11}}\boldsymbol{F}R(-\theta)\boldsymbol{m}\boldsymbol{m}^T R(\theta) & -\boldsymbol{I} & & \\ \vdots & \vdots & \ddots & \\ \frac{l_{N1}}{l_{11}}\boldsymbol{F}^{N-1}R(-\theta)\boldsymbol{m}\boldsymbol{m}^T R(\theta) & \boldsymbol{0} & \cdots & -\boldsymbol{I}\end{bmatrix}.$$

Here, $\boldsymbol{m}\boldsymbol{m}^T$ is a projection operator along the direction of $\boldsymbol{m}$, and $\boldsymbol{m}\boldsymbol{m}^T - \boldsymbol{I}$ yields a vector orthogonal to $\boldsymbol{m}$.

For $\boldsymbol{G}_{NA}$, first consider the kth inactive constraint at the current time (i.e., the kth row in $\boldsymbol{G}$):

$$\boldsymbol{G}_{NA}^k = \begin{bmatrix}\boldsymbol{k}^T R(\theta), & 0, & \cdots, & 0\end{bmatrix}$$
$$\boldsymbol{k}^T = \begin{bmatrix}\cos\frac{2k-1}{6}\pi, & \sin\frac{2k-1}{6}\pi\end{bmatrix}, \quad k \ne m.$$

The left-hand side of the inequality in (35) becomes

$$\begin{aligned}&\boldsymbol{G}_{NA}^k\left(\boldsymbol{H}^{-1}\boldsymbol{G}_A^T\boldsymbol{G}_A\frac{d_H}{l_{11}} - \boldsymbol{I}\right)\boldsymbol{H}^{-1}\boldsymbol{M}^T\boldsymbol{x}_0 \\ &= \boldsymbol{k}^T(\boldsymbol{m}\boldsymbol{m}^T - \boldsymbol{I})R(\theta - \omega T_s - \theta_B)\frac{p_1 s_F}{d_H s_B}\boldsymbol{x}_0.\end{aligned} \tag{36}$$

We also have

$$\boldsymbol{w}_{NA}^k = \frac{\sqrt{3}}{2}b - \boldsymbol{k}^T R(\theta)\bar{\boldsymbol{u}},\ \boldsymbol{G}_{NA}^k\boldsymbol{H}^{-1}\boldsymbol{G}_A^T = \frac{l_{11}}{d_H}\boldsymbol{k}^T\boldsymbol{m}$$

and the right-hand side of the inequality in (35) becomes

$$\begin{aligned}&\boldsymbol{w}_{NA}^k - \boldsymbol{G}_{NA}^k\boldsymbol{H}^{-1}\boldsymbol{G}_A\frac{d_H}{l_{11}}\boldsymbol{w}_A \\ &= \frac{\sqrt{3}}{2}b(1 - \boldsymbol{k}^T\boldsymbol{m}) + \boldsymbol{k}^T(\boldsymbol{m}\boldsymbol{m}^T - \boldsymbol{I})R(\theta)\bar{\boldsymbol{u}}.\end{aligned} \tag{37}$$

Combining (36) and (37), we get

$$\frac{p_1 s_F}{d_H s_B}\boldsymbol{k}^T(\boldsymbol{m}\boldsymbol{m}^T - \boldsymbol{I})R(\theta - \omega T_s - \theta_B)\left(\boldsymbol{x}_0 - \frac{d_H s_B}{p_1 s_F}R(\omega T_s + \theta_B)\bar{\boldsymbol{u}}\right) < \frac{\sqrt{3}}{2}b(1 - \boldsymbol{k}^T\boldsymbol{m})$$

which can be further simplified to

$$\cot\frac{k-m}{6}\pi\ \boldsymbol{m}^T R\left(\theta - \omega T_s - \theta_B + \frac{\pi}{2}\right)\left(\boldsymbol{x}_0 - \frac{d_H s_B}{p_1 s_F}R(\omega T_s + \theta_B)\bar{\boldsymbol{u}}\right) < \frac{d_H s_B}{p_1 s_F}\frac{\sqrt{3}}{2}b. \tag{38}$$

Equation (38) defines a half-plane, and different k generates parallel line that is orthogonal to the magenta edge defined by (34). When $|k - m| = 3$, the line vanishes. When $k - m = 1$ or $k - m = 5$, $|\cot\frac{k-m}{6}\pi|$ achieves maximum value and these two lines define the boundaries of the critical region shown as green line segments in Fig. 2(b), and they are perpendicular to the magenta edge.

Next consider the kth inactive constraint at the next sampling instant (i.e., the $(k+6)$th row in $\boldsymbol{G}$)

$$\boldsymbol{G}_{NA}^k = \begin{bmatrix}0, & \boldsymbol{k}^T R(\theta + \omega T_s), & \cdots, & 0\end{bmatrix}$$
$$\boldsymbol{k}^T = \begin{bmatrix}\cos\frac{2k-1}{6}\pi, & \sin\frac{2k-1}{6}\pi\end{bmatrix}, k \ne m. \tag{39}$$

Then, we have

$$\begin{aligned}&\boldsymbol{G}_{NA}^k\left(\frac{\boldsymbol{H}^{-1}\boldsymbol{G}_A^T\boldsymbol{G}_A}{\boldsymbol{G}_A\boldsymbol{H}^{-1}\boldsymbol{G}_A^T} - \boldsymbol{I}\right)H^{-1}\boldsymbol{M}^T\boldsymbol{x}_0 \\ &= \left(\frac{p_1 l_{21}}{l_{11}}\boldsymbol{k}^T\boldsymbol{m}\boldsymbol{m}^T - p_2\boldsymbol{k}^T\right)\frac{s_F^2}{s_B d_H}R(\theta - \omega T_s - \theta_B)\boldsymbol{x}_0.\end{aligned} \tag{40}$$

The right-hand side of the inequality in (35) becomes

$$\boldsymbol{w}_{NA}^{k} = \frac{\sqrt{3}}{2}b - \boldsymbol{k}^T R(\theta + \omega T_s)\bar{\boldsymbol{u}}$$

$$\boldsymbol{G}_{NA}^{k}\boldsymbol{H}^{-1}\boldsymbol{G}_A^T = \frac{l_{21}s_F}{d_H}\boldsymbol{k}^T\boldsymbol{m}$$

which leads to

$$\boldsymbol{w}_{NA}^{k} - \boldsymbol{G}_{NA}\boldsymbol{H}^{-1}\boldsymbol{G}_A\frac{d_H}{l_{11}}\boldsymbol{w}_A = \frac{\sqrt{3}}{2}b - \boldsymbol{k}^T R(\theta + \omega T_s)\bar{\boldsymbol{u}} - \frac{l_{21}s_F}{l_{11}}\left(\frac{\sqrt{3}}{2}b - \boldsymbol{m}^T R(\theta)\bar{\boldsymbol{u}}\right)\boldsymbol{k}^T\boldsymbol{m}. \tag{41}$$

We can show when $\boldsymbol{k} = \boldsymbol{m}$, it generates the smallest area. Combining (40) and (41), we have

$$\boldsymbol{m}^T R(\theta - \omega T_s - \theta_B + \pi)\left(\boldsymbol{x}_0 + \frac{l_{11}}{l_{21}}\boldsymbol{F}^{-2}\boldsymbol{B}\bar{\boldsymbol{u}} - \boldsymbol{F}^{-1}\boldsymbol{B}\bar{\boldsymbol{u}}\right) < \frac{s_B}{s_F^2}\left(s_F - \frac{l_{11}}{l_{21}}\right)\frac{\sqrt{3}}{2}b.$$

Comparing with (34), we know that this defines a line that is parallel to the magenta edge of the innermost hexagon, which is plotted as the black line in Fig. 2(b). Now the magenta, green, and black lines form a rectangular critical region corresponding to the active set $\{1\}$.

The control input $\boldsymbol{V}_0^*$ can be obtained as

$$\boldsymbol{V}_0^* = -\boldsymbol{H}^{-1}\boldsymbol{M}^T\boldsymbol{x}_0 + \boldsymbol{\mu}^* = -\boldsymbol{H}^{-1}\boldsymbol{M}^T\boldsymbol{x}_0 - \boldsymbol{H}^{-1}\boldsymbol{G}_A^T\boldsymbol{\lambda}_A$$

$$\boldsymbol{\lambda}_A^* = -\frac{\boldsymbol{w}_A + \boldsymbol{S}_A\boldsymbol{x}_0}{\boldsymbol{G}_A\boldsymbol{H}^{-1}\boldsymbol{G}_A^T} = -\frac{\boldsymbol{w}_A + \boldsymbol{G}_A\boldsymbol{H}^{-1}\boldsymbol{M}^T\boldsymbol{x}_0}{l_{11}/d_H}.$$

As MPC applies only the control input at the current sampling instant, we have

$$\boldsymbol{v}_0^* = \frac{-p_1}{d_H}\boldsymbol{B}^{-1}\boldsymbol{F}\boldsymbol{x}_0 + \boldsymbol{\mu}_0^* = \frac{-p_1}{d_H}\boldsymbol{B}^{-1}\boldsymbol{F}\boldsymbol{x}_0^* \tag{42}$$

where $\boldsymbol{x}_0^* = \boldsymbol{x}_0 - \frac{d_H}{p_1}\boldsymbol{F}^{-1}\boldsymbol{B}\boldsymbol{\mu}_0^*$. It is easy to show that $\boldsymbol{x}_0^*$ is on the magenta hexagon edge and $\boldsymbol{x}_0^* - \boldsymbol{x}_0$ is the dashed line that is parallel to blue spoke lines as shown in Fig. 2.

Furthermore, the control performance, especially the transient response is related to N by the pole location of the closed-loop system. When none of the constraints active, the optimal control $\boldsymbol{v}_0^*$ can be treated as a state feedback law $\boldsymbol{v}_0^* = -p_1/d_H\boldsymbol{F}\boldsymbol{B}^{-1}\boldsymbol{x}_k$. Thus, the closed-loop system becomes

$$\boldsymbol{x}_{k+1} = \boldsymbol{F}\boldsymbol{x}_k + \boldsymbol{B}\boldsymbol{v}_0^* = (1 - p_1/d_H)\,\boldsymbol{F}\boldsymbol{x}_k. \tag{43}$$

The poles of this system are $(1 - p_1/d_H)s_F(\cos\omega T_s \pm \mathrm{j}\sin\omega T_s)$, and thus smaller magnitude of the closed-loop system poles $(1 - p_1/d_H)s_F$ yields faster convergent dynamics. In Fig. 3, we numerically illustrates the relationship between the magnitude and the prediction horizon N for different values of the penalty parameter r. The results demonstrate that as the prediction horizon length increases, the magnitude increases across all values of r, indicating improved convergence performance with a longer prediction horizon. However, it also shows that the reduction in $(1 - p_1/d_H)s_F$ becomes marginal as N exceeds a certain threshold $N = 10$.

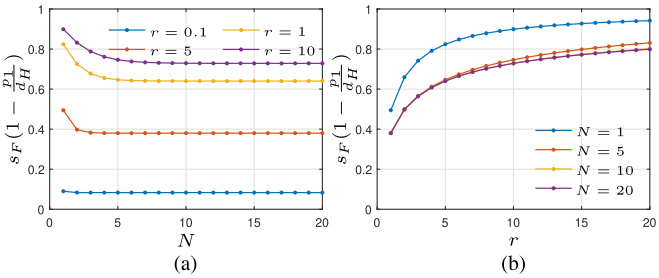

Fig. 3. Magnitude of the closed-loop system poles versus (a) different prediction horizon N and (b) different control penalty r.

TABLE I
SPECIFICATIONS FOR THE SPMSM USED IN BOTH SIMULATION AND EXPERIMENTS

Stator resistance R_s	6.7 Ω	Rated power	100 W
D-axis inductance L_d	9 mH	Rated current	1.0 A
Q-axis inductance L_q	9 mH	Maximum current	1.5 A
Back EMF constant ψ_f	0.037 V · s	Rated speed	50 Hz
Pole pairs p	4	Rated dc-link voltage	150 V

V. Simulation and Experimental Results

In this section, we show the simulation and experimental results.

A. Simulation Results

Our algorithm provides an efficient way of solving the constrained optimization problem resulting from the MPC formulation. We perform numerical simulations to show that it yields the same optimal solutions as those from standard optimization solvers.

Consider a 100 W servo motor with the specifications listed in Table I. We conduct simulations of the current control, where the reference trajectories for i_d and i_q are given, and the MPC algorithm needs to determine the voltage commands at each sampling instant. In particular, we set the motor currents i_d and i_q to track step inputs from 0A to 0.5A at 0.01s and back to 0A and −1A at 0.02s, respectively. The prediction horizon is set to $N = 10$ and control penalty weight to $r = 10$. At each sampling instant, the optimal solution for (23) is computed by both our algorithm and MATLAB `quadprog` command. Fig. 4(a) displays the current reference commands and output responses, whereas Fig. 4(b) shows the corresponding voltage controls. Since it is critical to assess cases of saturation, Fig. 4(c) plots the voltage controls in the $\alpha\beta$-frame, revealing that immediately after the reference command changes, the control signals saturate along the edges of the SVPWM hexagon. Finally, Fig. 4(d) shows the difference of these two methods, which is within the numerical accuracy. This simulation confirms that our algorithm produces the same optimal solution as MATLAB optimization toolbox.

B. Experimental Results

For the experiments, we again use the motor with the specifications listed in Table I, and the experimental platform is shown

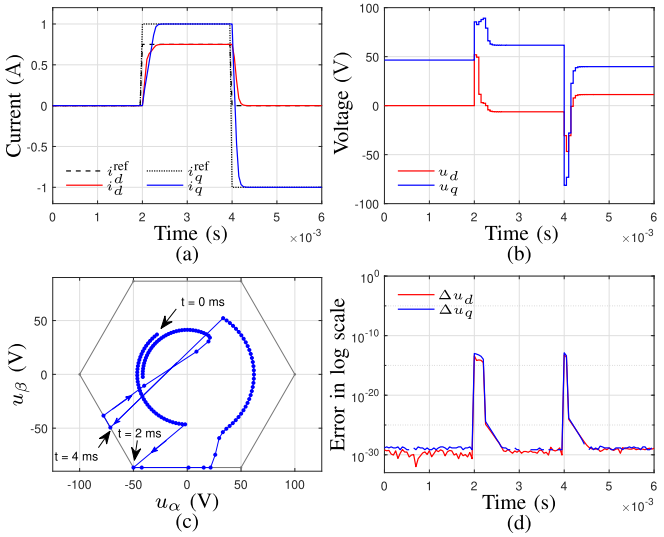

Fig. 4. Optimization results from our MPC algorithm vs those from MATLAB `quadprog` command. (a) The current reference commands and output responses; (b) The obtained voltage controls in the time domain; (c) The voltage controls in $\alpha\beta$-frame; and (d) The difference between two methods (data points with values at 0 are not shown).

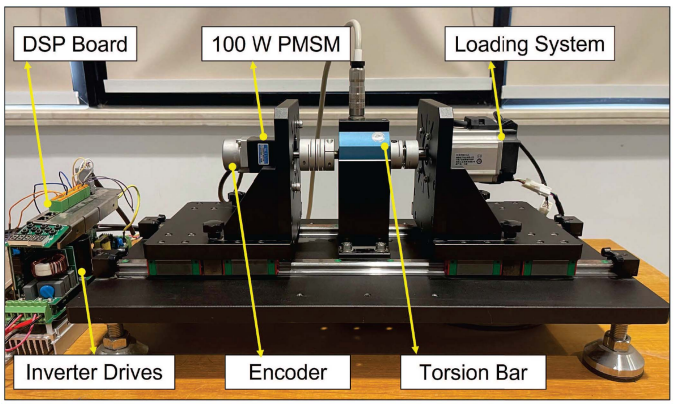

Fig. 5. Experimental platform of the PMSM drives.

in Fig. 5. Another servo PMSM drive is used as a high dynamic loading system, capable of operating in either pure loading or speed control mode. The MPC algorithm is implemented on a DSP board integrated with a low-cost Micro Control Unit (MCU) SPC2168, priced at around 1 USD each [24]. Phase currents are measured by sampling circuits on the DSP board with 16 kHz sampling frequency, whereas the rotor position is measured by a 17-bit absolute encoder. Dead-time effects and inverter nonlinearities are compensated by the hybrid VSI error model-based method described in [25].

Time delays, particularly computation delays, are common in engineering applications, often resulting in a one sample period delay between computation and execution of control inputs. This can degrade system performance, especially in high-precision, fast-dynamics applications. To address this, we use a delay compensation strategy for the MPC from [19], where the current at the next instant is predicted and used as the starting point for

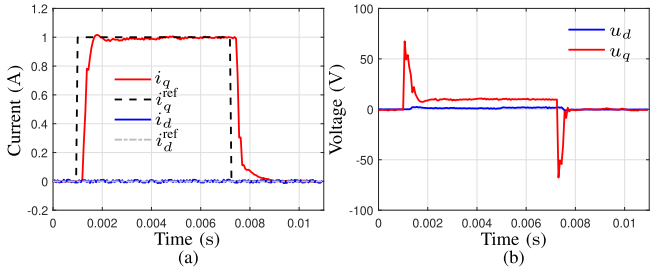

Fig. 6. Stator current tracking at standstill from our MPC algorithm. (a) d- and q-axis currents tracking; (b) control signals u_d and u_q.

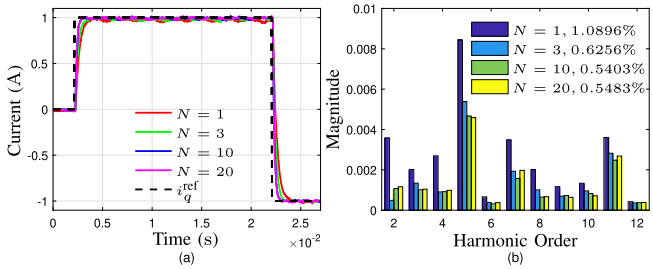

Fig. 7. Effects of the prediction horizon N on (a) transient performance and (b) spectrum distribution of steady-state currents.

MPC optimization. The optimal control law is then computed based on this prediction and applied at the next time instant.

First, we present the current tracking performance of our explicit MPC algorithm when the motor speed is controlled at zero in Fig. 6, with parameters set to $N = 10$ and $r = 10$. [1] The d-axis current is regulated at 0 A, while the q-axis current tracks a step input from 0 A to 1.0 A, followed by a return to 0 A. The results show prompt current response with no steady-state error.

Subsequently, we evaluate the control performance of the proposed controller with different prediction horizons $N = 1, 3, 10, 20$ in Fig. 7. The experimental results demonstrate that the current transient becomes significantly faster as the prediction horizon increases, together with better THD performance. This improvement highlights the benefit of a longer prediction horizon in achieving better dynamic performance. In addition, we observe that the dynamic response for $N = 20$ is almost identical to that of $N = 10$. This finding again confirms that increasing N beyond a certain value offers limited returns in terms of performance improvement, which aligns well with the theoretical analysis discussed in Section IV.

We also perform experiments under varying operating conditions where the motor currents track $i_d = 0$ A and $i_q = 0.3$ A, 0.7 A, 1.0 A while the motor operates at 100 and 200 Hz. These results, shown in Fig. 8, demonstrate good tracking performance across all cases. In addition, we show the current tracking performances when the motor follows a speed profile in Fig. 9(a), and when being subjected to a load change in Fig. 9(b). At $t = 0.06$ s, the load torque steps up from 0.06 to 0.12 N·m, and thus the

[1] As the regular N_i-polygon approximates the outermost boundary in Fig. 2 without affecting solver performance due to geometric projection, we simplify by using a circular current constraint corresponding to N_i goes to infinity.

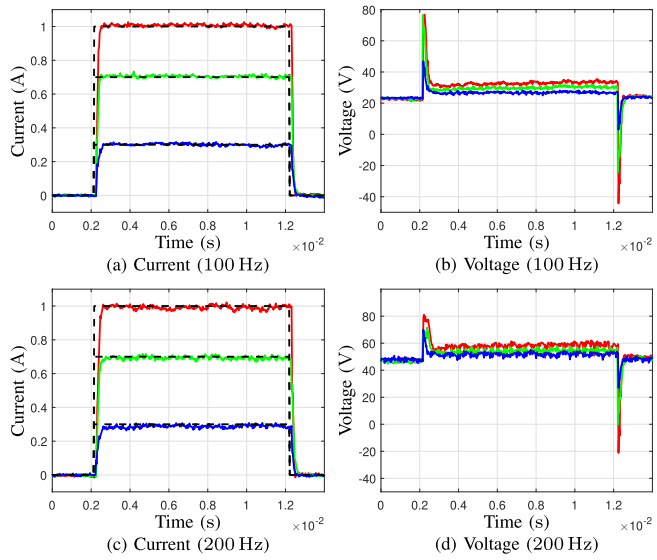

Fig. 8. Stator current tracking for the motor operating at 100 Hz (top row) and 200 Hz (bottom row). The red, green, and blue lines represent the tracking of reference trajectories (indicated by dashed lines) from 0 A to 1.0 A, 0.7 A, 0.3 A, and back to 0 A, respectively.

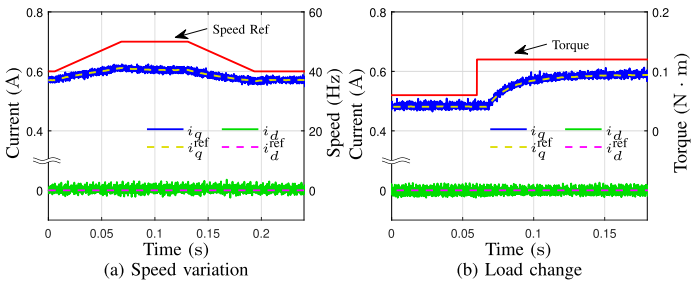

Fig. 9. Current tracking performances when the motor is (a) to follow a speed profile, and (b) subject to a load change.

q-axis reference increases to compensate for the additional load. We observe that the achieved q-axis current closely tracks the reference due to the prompt dynamics of the proposed current controller. Meanwhile, the d-axis current remains at zero as desired. In addition, it is worthy to mention that we utilized a disturbance observer with a feed-forward compensation mechanism in our experiments to reject the internal and external disturbance such that the proposed MPC can achieve offset-free tracking performance reference.

In Fig. 10, we illustrate the control performance under active current constraints. From $t = 0$ ms to $t = 15$ ms, a step change is applied to the q-axis current reference, following the sequence from 1 to 1.2 A and finally settling at 1.7 A, while the d-axis current is maintained at 0 A. Under normal operating conditions, the current reference is set within the current limitation circle, which corresponds to $\|\boldsymbol{i}^{\text{ref}}\|_2 \leq 1.5$ A. However, we intentionally set the current reference to 1.7 A in Fig. 10 to demonstrate how our controller handles cases of current constraint violation. Since $I_{\text{ref}} > I_{\max} = 1.5$ A, the original optimization problem becomes infeasible. To address this issue, our controller performs

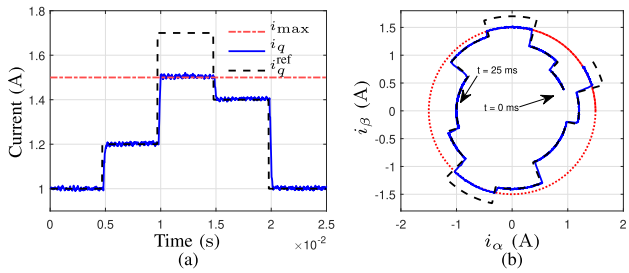

Fig. 10. Experimental results under active current constraints. (a) Current trajectories in the dq-frame in the time domain. (b) Current trajectories in the i_α-i_β-plane.

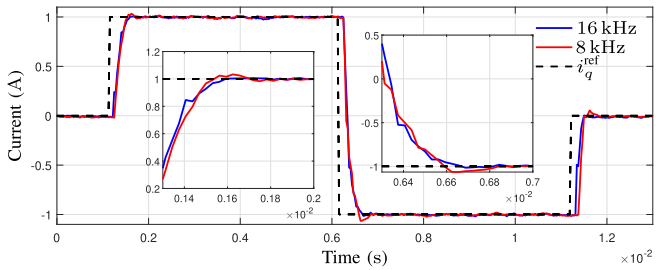

Fig. 11. Experimental comparison of the current tracking performances under sampling frequency $f_s = 8$ kHz and $f_s = 16$ kHz.

a geometric projection to drag $\boldsymbol{i}^{\text{ref}}$ onto the boundary of the current limitation circle, as discussed in Section IV-A. As seen in Fig. 10(a), when the current reference is less than or equal to maximum current value, the controller exhibits superior tracking performance; however, when the current reference is set beyond the current limitation, the current response will stay at maximum allowable value at steady state. Fig. 10(b) further shows the current trajectories on the i_α-i_β-plane.

Now, we evaluate the proposed MPC solver performance under different sampling frequencies. In Fig. 11, the sampling frequency of the compared experiment is set to 8 kHz, with the prediction horizon N and regularization parameter r unchanged. The experimental results show that a lower sampling frequency can degrade transient performance, particularly causing larger overshoots. This is because the control frequency matches the sampling frequency, so reduced sampling lowers the update rate, limiting the controller's responsiveness. Conversely, higher sampling frequencies enable more frequent updates, enhancing transient response and precision in tracking reference signals.

In the following, we compare the current tracking performance of the MPC algorithm with a PI controller, e.g., the analytical discrete-time pole-placement design method presented in [4]. Although the objective of this article is not to demonstrate the performance advantages of MPC over PI, we include these comparison experiments for completeness. We set $N = 10$ and $r = 10$ for MPC, while the PI controller is tested with bandwidths of 2.0, 2.2, 2.4, and 2.6 kHz. Fig. 12(a) shows the q-axis currents for both the MPC and PI controllers, while (b) and (c) display the three-phase currents. For clarity, only the currents from the PI controller with bandwidth 2.2 kHz are shown in

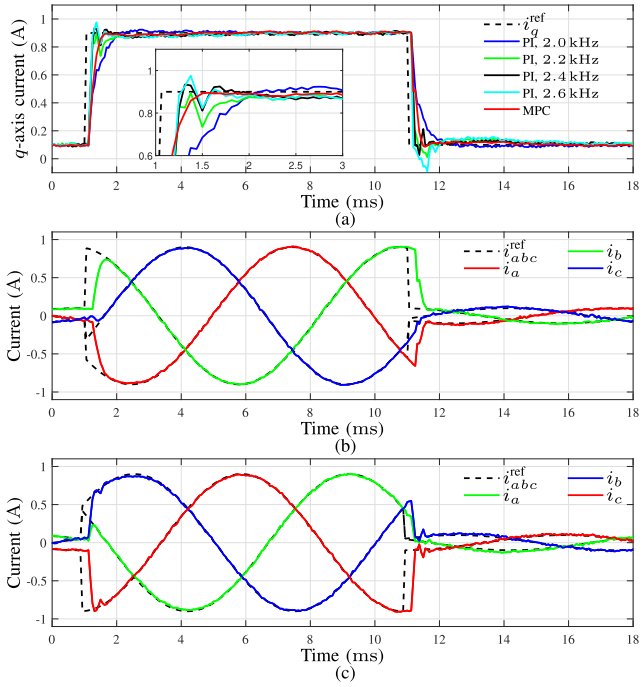

Fig. 12. (a) Transient response comparison between our MPC and the advanced discrete-time pole-placement PI controller in [4]; (b) three-phase currents from MPC; and (c) three-phase currents from PI with bandwidth 2.2 kHz.

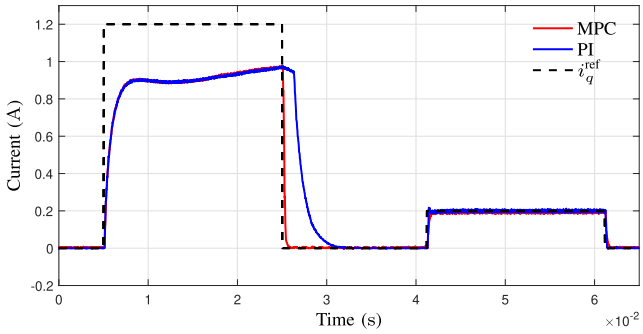

Fig. 13. Experimental comparison between the proposed MPC with the traditional PI method under control saturation.

(c). As can be seen, MPC has a clear advantage in balancing fast response with minimal overshoot. While PI controllers with higher bandwidths can match the response speed of MPC, they tend to exhibit significant overshoots and undershoots. Conversely, lower-bandwidth PI controllers reduce overshoot but are noticeably slower than MPC. Note that the performance of the PI controller can be further enhanced through fine-tuning and incorporating additional features.

We then compare the control performance of the proposed MPC with the PI-based controller under control saturation. In Fig. 13, we intentionally reduced the dc-link voltage to 30% of its original value, imposing a stringent voltage constraint on both controllers. As anticipated, due to the limited available voltage, both controllers exhibit control saturation and are unable to drive the current to the desired reference value. At $t = 25$ ms, the current reference suddenly steps down to 0A. Despite being initially

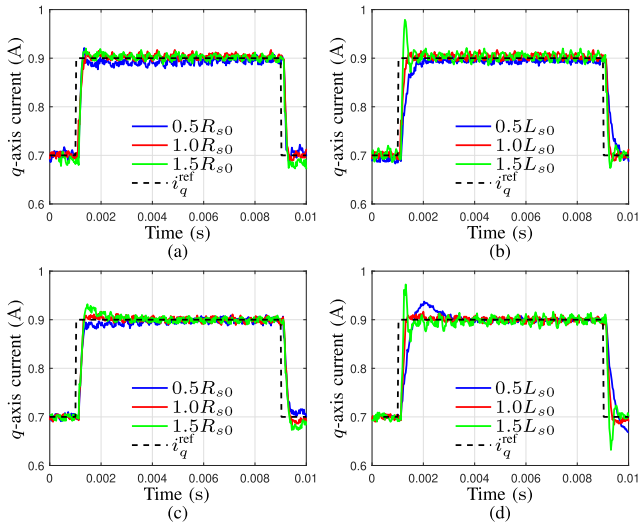

Fig. 14. Robustness evaluations for our MPC algorithm and PI controller, when subject to parameter variations. (a) MPC with stator resistance variations; (b) MPC with inductance variations; (c) PI with stator resistance variations; and (d) PI with inductance variations.

constrained by the voltage limit, our method efficiently exits the saturation region and quickly adjusts to the new unconstrained voltage command, resulting in a rapid response and accurate tracking of the new reference. In contrast, the PI-based controller exhibits sluggish behavior due to integrator windup.

In Fig. 14, we evaluate the robustness performance of our MPC algorithm together with PI controller, when subject to model parameter variations. For MPC, set $N = 10$ and $r = 10$. Take nominal values of stator resistance R_{s0} and inductance L_{s0} as those shown in Table I, and their real values may deviate from the nominal ones when the motor works at different operating conditions. Fig. 14(a) shows the current tracking performance from our MPC algorithm when the stator resistance is taken as $0.5R_{s0}$, R_{s0}, and $1.5R_{s0}$, and Fig. 14(b) the results when the inductance is taken as $0.5L_{s0}$, L_{s0}, and $1.5L_{s0}$, respectively. Fig. 14(c) and (d) is the corresponding results for PI controller. We observe that larger resistance and smaller inductance produce faster transient response, but they all yield quite similar dynamic responses. PI controller produces acceptable robustness performance, with slightly larger overshoots in some cases.

Now we compare the control performance of the proposed MPC with the analytical-solution-based solver aVsIs [21], fast solver from [26], and the decaying amplification aggregation MPC (DAA-MPC) [27]. The recommended parameter setting are adopted for the aVsIs, fast solver in [26], and DAA-MPC in Fig. 15. For aVsIs, only the first time step is considered in both the constraint and cost functions, meaning that the control and prediction horizons are set to $N = 1$. In contrast, our method accounts for both future states and control actions with $N = 10$. While both aVsIs and our method use a similar geometric projection approach for the first step constraint, achieving comparable dynamic responses to reference step changes, aVsIs shows significant overshoots when responding to both step-up and step-down reference signal changes, whereas our method

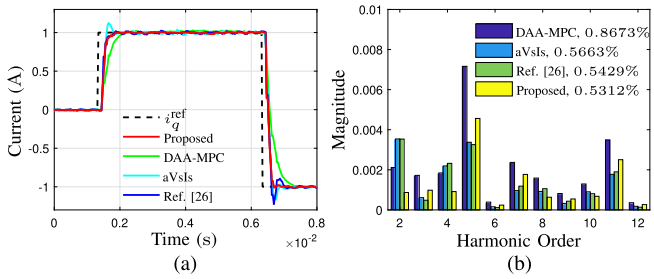

Fig. 15. Experimental comparison for the proposed MPC, aVsIs [21], Fast Solver in Ref. [26], and DAA-MPC [27] on (a) transient control performance and (b) spectrum distribution of steady-state currents.

TABLE II
TRANSIENT AND STEADY-STATE PERFORMANCE COMPARISON

	Proposed	aVsIs	DAA -MPC	PI (2.6 kHz)	Ref. [26]
Overshoot (%)	1.4	12.6	2.3	8.9	9.1
Settling time (ms)	6.0	4.0	9.2	10.0	4.2
THD (%)	0.53	0.57	0.87	0.65	0.54

TABLE III
COMPARISON OF COMPUTATIONAL TIMES (μs)

No. of active constraints	0	1	2	3	4
Proposed MPC	3.45	3.55	3.60	3.45	3.50
EMPC in [23]	4.05	4.75	7.45	10.25	25.15
aVsIs in [21]	4.15				
Solver in [26]	4.60				
DAA-MPC in [27]	6.85				
Decoupled PI in [4]	1.75				

exhibits almost no overshoot. This difference can be primarily attributed to the longer prediction and control horizons used in our approach. The fast solver from [26], on the other hand, shows a small overshoot comparable to our method for the step-up response, but a large overshoot for the step-down response.

Meanwhile, the DAA-MPC is a modification of traditional explicit MPC, incorporating a decaying amplification aggregation strategy to extend the prediction horizon without introducing exponential complexity. The results in Fig. 15 show that both the DAA-MPC and our method exhibit no significant overshoot during reference step-up and step-down changes, due to the use of long prediction horizons in both approaches. However, the proposed method demonstrates a faster transient response, as the DAA-MPC can only provide a suboptimal solution due to its formulation.

Moreover, Table II summarizes the transient and steady-state performance indices of these controllers. Overshoot and settling time evaluate transient performance, while THD reflects harmonic content and noise levels in the steady-state current. The overshoot is averaged over both step-up and step-down stages. The reduced overshoot and lower THD highlight the superior overall performance of our proposed method.

Last, Table III lists the computational times for our proposed MPC, the EMPC method from [23], the aVsIs method [21], and the DAA-MPC [27] method on the MCU in experiments. These results are shown for cases with 0, 1, $\cdots$, and 4 active constraints. Here, the DSP board is configured to perform only these computations, without controlling the motor. Notably, our MPC method maintains a nearly constant computational time of approximately 3.5 μs, regardless of the number of active constraints. In contrast, the times for EMPC increase significantly as the number of constraints grows. Moreover, the average computational times for the aVsIs and DAA-MPC are approximately 4.15 and 6.85 μs, respectively. While both aVsIs and DAA-MPC offer computational efficiency for normal industrial drives, the proposed MPC can deliver an analytical solution with a longer prediction horizon, resulting in superior control performance. For reference, the real-time control sampling period in previous experiments is 66 μs.

VI. CONCLUSION

In this article, we derived analytic solutions for explicit MPC applied to current control of SPMSM drives. We showed a simple geometric representation of the MPC algorithm, which facilitates ease of engineering implementation. Experimental results demonstrate that the proposed MPC algorithm delivers fast dynamic response and is computationally efficient, making it suitable for both high-speed servo systems and cost-sensitive applications.

The proposed MPC algorithm can be further extended to Interior permanent magnet synchronous motor drives. These results will be presented in an ensuing paper. Moreover, due to similar mathematical model and modulator constraints, we are implementing this technique to other power electronics applications such as static synchronous compensator, and grid-connected converters in distributed generation system.

REFERENCES

[1] G. Wang, G. Zhang, and D. Xu, *Position Sensorless Control Techniques for Permanent Magnet Synchronous Machine Drives*. Berlin, Germany: Springer, 2020.
[2] S. Vaez-Zadeh, *Control of Permanent Magnet Synchronous Motors*. London, U.K.: Oxford Univ. Press, 2018.
[3] Z. Q. Zhu and X. M. Wu, *Sensorless Control of Permanent Magnet Synchronous Machine Drives*. Hoboken, NJ, USA: Wiley-IEEE Press, 2023.
[4] M. Hinkkanen, H. A. A. Awan, Z. Qu, T. Tuovinen, and F. Briz, "Current control for synchronous motor drives: Direct discrete-time pole-placement design," *IEEE Trans. Ind. Appl.*, vol. 52, no. 2, pp. 1530–1541, Mar./Apr. 2016.
[5] P. Karamanakos, E. Liegmann, T. Geyer, and R. Kennel, "Model predictive control of power electronic systems: Methods, results, and challenges," *IEEE Open J. Ind. Appl.*, vol. 1, pp. 95–114, 2020.
[6] J. Rodriguez et al., "State of the art of finite control set model predictive control in power electronics," *IEEE Trans. Ind. Inform.*, vol. 9, no. 2, pp. 1003–1016, May 2013.
[7] M. Preindl and S. Bolognani, "Model predictive direct torque control with finite control set for PMSM drive systems, Part 1: Maximum torque per ampere operation," *IEEE Trans. Ind. Inform.*, vol. 9, no. 4, pp. 1912–1921, Nov. 2013.
[8] P. Karamanakos, T. Geyer, and R. P. Aguilera, "Long-horizon direct model predictive control: Modified sphere decoding for transient operation," *IEEE Trans. Ind. Appl.*, vol. 54, no. 6, pp. 6060–6070, Nov./Dec. 2018.
[9] D. Xiao, K. S. Alam, M. Norambuena, M. F. Rahman, and J. Rodriguez, "Modified modulated model predictive control strategy for a grid-connected converter," *IEEE Trans. Ind. Electron.*, vol. 68, no. 1, pp. 575–585, Jan. 2021.

[10] Q. Yang et al., "Computationally efficient fixed switching frequency direct model predictive control," *IEEE Trans. Power Electron.*, vol. 37, no. 3, pp. 2761–2777, Mar. 2022.
[11] E. Zafra, S. Vazquez, T. Geyer, R. P. Aguilera, E. Freire, and L. G. Franquelo, "Computational analysis of the long horizon FCS-MPC problem for power converters," *IEEE Trans. Power Electron.*, vol. 39, no. 10, pp. 12762–12773, Oct. 2024.
[12] S. Hanke, O. Wallscheid, and J. Böcker, "Continuous-control-set model predictive control with integrated modulator in permanent magnet synchronous motor applications," in *Proc. IEEE Int. Electric Machines Drives Conf.*, IEEE, 2019, pp. 2210–2216.
[13] O. Wallscheid and E. F. B. Ngoumtsa, "Investigation of disturbance observers for model predictive current control in electric drives," *IEEE Trans. Power Electron.*, vol. 35, no. 12, pp. 13563–13572, Dec. 2020.
[14] M. Rossi, P. Karamanakos, and F. Castelli-Dezza, "Indirect model predictive control for a grid-tied three-level neutral point clamped converter with an LCL filter," in *Proc. IEEE Energy Convers. Congr. Expo.*, IEEE, 2020, pp. 6245–6252.
[15] A. Bemporad, M. Morari, V. Dua, and E. N. Pistikopoulos, "The explicit linear quadratic regulator for constrained systems," *Automatica*, vol. 38, no. 1, pp. 3–20, 2002.
[16] A. Linder and R. Kennel, "Model predictive control for electrical drives," in *Proc. IEEE 36th Power Electron. Specialists Conf.*, IEEE, 2005, pp. 1793–1799.
[17] S. Bolognani, S. Bolognani, L. Peretti, and M. Zigliotto, "Design and implementation of model predictive control for electrical motor drives," *IEEE Trans. Ind. Electron.*, vol. 56, no. 6, pp. 1925–1936, Jun. 2009.
[18] S. Mariethoz, A. Domahidi, and M. Morari, "High-bandwidth explicit model predictive control of electrical drives," *IEEE Trans. Ind. Appl.*, vol. 48, no. 6, pp. 1980–1992, Nov./Dec. 2012.
[19] F. Borrelli, A. Bemporad, and M. Morari, *Predictive Control for Linear and Hybrid Systems*. Cambridge, U.K.: Cambridge Univ. Press, 2017.
[20] C. Dirscherl, C. M. Hackl, and K. Schechner, "Explicit model predictive control with disturbance observer for grid-connected voltage source power converters," in *Proc. IEEE Int. Conf. Ind. Technol.*, 2015, pp. 999–1006.
[21] I. D. De Martin, D. Pasqualotto, and F. Tinazzi, "aVsIs: An analytical-solution-based solver for model-predictive control with hexagonal constraints in voltage-source inverter applications," *IEEE Trans. Power Electron.*, vol. 37, no. 12, pp. 14375–14383, Dec. 2022.
[22] I. D. De Martin, A. Brosch, F. Tinazzi, and M. Zigliotto, "Continuous control set model predictive torque control with minimum current magnitude criterion for synchronous motor drives," *IEEE Trans. Ind. Electron.*, vol. 71, no. 7, pp. 6787–6796, Jul. 2024.
[23] G. Cimini, D. Bernardini, S. Levijoki, and A. Bemporad, "Embedded model predictive control with certified real-time optimization for synchronous motors," *IEEE Trans. Control Syst. Technol.*, vol. 29, no. 2, pp. 893–900, Mar. 2021.
[24] "SPC2168 product introduction," SPINTROL Company Ltd, 2024. [Online]. Available: http://www.spintrol.com/index/index/product2/id/25.html
[25] B. Xia, X. Gao, J. Zhang, and M. Zhang, "Automated identification of a hybrid VSI error model for PMSM drives," *IEEE Trans. Power Electron.*, vol. 39, no. 12, pp. 15982–15993, Dec. 2024.
[26] A. Favato et al., "Fast solver for implicit continuous set model predictive control of electric drives," *IEEE Access*, vol. 10, pp. 17430–17440, 2022.
[27] W. Chen, D. Li, Y. Xi, Y. Xu, and Z. Gan, "The research of grid-connected inverter control based on decaying amplification aggregation strategy in predictive control," *Cluster Comput.*, vol. 22, pp. 6633–6646, 2019.

Jun Zhang received the B.S. degree in automatic control from Shanghai Jiao Tong University, Shanghai, China, in 1993, and the M.S. and Ph.D. degrees in electrical engineering from the University of California at Berkeley, CA, USA, in 1999 and 2003, respectively.

After that he worked at several high tech firms in the Silicon Valley. He is currently a Professor with the UMich-SJTU Joint Institute in Shanghai Jiao Tong University. His research interests include motion control and complex system control.

Binyu Xia received the B.S. degree in electronic and computer engineering, in 2021, from Shanghai Jiao Tong University, Shanghai, China, where he is currently working toward the Ph.D. degree in automatic control.

His current research interests include electric machine control and other advanced control strategies.

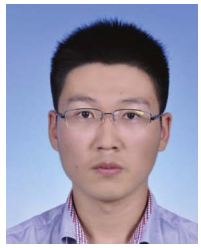

Mingming Zhang (Member, IEEE) received the B.S. degree in mechanical engineering from East China University of Science and Technology, Shanghai, China, in 2015, the M.S. degree in mechanical engineering and the Ph.D degree in control science and engineering both from Shanghai Jiao Tong University, Shanghai, China, in 2019 and 2022, respectively.

He is currently a Postdoctoral Researcher with the Global Institute of Future Technology, Shanghai Jiao Tong University. His research interests include grid-connected converter control and motion control.